Large-Eddy Simulation of a Flow Generated by a Piston-driven Synthetic Jet Actuator

Tung Duy Pham[1], Tomoaki Watanabe[2,*], Koji Nagata[3]

[1] Department of Aerospace Engineering, Nagoya University, Nagoya 464-8603, Japan
[2] Education and Research Center for Flight Engineering, Nagoya University, Nagoya 464-8603, Japan
[3] Department of Mechanical Engineering and Science, Kyoto University, Kyoto 615-8530, Japan

ARTICLE INFO	ABSTRACT
	We study the characteristics of a compressible flow generated by a piston-driven synthetic jet actuator by employing large-eddy simulation with OpenFOAM. The actuator consists of a piston and a cylinder with a square orifice on top and produces a compressible synthetic jet with the piston movement. Comparison with experimental data demonstrates that the numerical model constructed with OpenFOAM is useful to examine the performance of the actuator. As the piston frequency increases, the maximum pressure inside the cylinder increases while the minimum pressure decreases. The fluid temperature inside the cylinder also varies similarly to the pressure. The maximum jet Mach number is well represented as a function of the maximum pressure. The phase-averaged velocity field of the synthetic jet confirms that the blowing and suction phases do not perfectly match with the piston movement. The root-mean-square velocity defined with the phase average also shows that a high turbulence level is observed in the region where the flow is decelerated at the furthest location of the jet in the blowing phase.

1. Introduction

Flow control is mostly based on two key strategies, which are passive control and active control. The passive one does not require any external energy. One of the examples of passive flow control is a boundary-layer separation control with vortex generators [1-3], which are often utilized for aerodynamics applications. On the other hand, the active flow control mostly utilizes actuators that are operated with power input. Moving objects, plasma, or electromagnetic are often used as an actuator in active control [4]. These methods inevitably have inherent trade-offs in fabrication methods, robust system-level, or design optimization. Recently, one of the typical methods is to employ piezoelectric synthetic jet actuators (SJAs) with a vibrating membrane [5,6]. The synthetic jet is found to be effective for flow control by modifying the velocity and vorticity distributions [7]. Because of the efficient heat transfer associated with turbulence, the synthetic jet actuator is applied as a cooling device [8,9]. It also can increase the overall lift/drag ratio of a cylinder [10] by interacting

* *Corresponding author.*
E-mail address: watanabe.tomoaki@c.nagoya-u.jp (Tomoaki Watanabe)

with a cross-flow [11]. The maximized effectiveness of SJAs is achieved when the cavity and diaphragm are at a coupled resonance. With a cross-flow of a gas turbine combustor, the SJAs enhance the mixing of flows at different temperatures by the wake structure [12]. The control of separated flows in diffusers with SJAs is also tested with numerical simulations [13].

Another prominent example of active control is a plasma actuator, including dielectric barrier discharge (DBD) [4]. The plasma actuator has advantages in its simple structure with no moving parts and fast response. It employs a pair of electrodes in an asymmetric layout and has been used for separation control over an airfoil [14-16]. The improvement of DBD plasma actuators is continuing to build their design such as applied voltage, pulsed frequencies, and exposed dielectric thickness [17-20]. Recent research [21] investigated the effect of pulsed actuation on the size of vortices, and the improvement through the pulsed actuation is compared with the steady counterpart. However, an induced flow by these DBD plasma actuators is generally slow, while typical flow speeds around practical airfoils are transonic or supersonic. Based on the velocity profile above a DBD actuator, the maximum streamwise velocity is smaller than 6.0 m/s for different cases of voltage or single, dual and triple actuators [18,19,21]. By increasing the voltage up to 30 kW, the ionic wind velocity can be up to 7.1 m/s [22]. Generally, the induced velocity by a DBD plasma actuator does not exceed 8 m/s [23]. Therefore, the velocity range of jets induced by conventional SJAs and DBD plasma actuators is not high enough to control high-speed flows.

A piston synthetic jet actuator (PSJA) is one of the candidates that can solve the problems by extending the velocity range of SJAs to a high-speed regime [24]. Instead of a piezoelectrically driven diaphragm, a piston in a cylinder is used to generate synthetic jets. In the original PSJA developed by Crittenden and Glezer [24], a piston driven by a DC motor generates synthetic jets from an orifice hole at the top of the cylinder. The jet velocity generated by the PSJA can be very high because the stroke length of the piston is much larger than the amplitude of diaphragm vibration of the conventional SJAs. Therefore, a supersonic flow can be generated by the PSJA at a high actuation frequency [24]. A bench-test PSJA actuator by Traub *et al.,* [25] with different slots sizes and piston frequencies marked the linear increase in the jet velocity with an increase in frequency. More recently, Eri *et al.,* [26] developed a novel PSJA with an auxiliary air inlet which noticeably improved the mass flow. The flow control with PSJA was also tested at laboratory scales. Gilarranz *et al.,* [27] have developed a PSJA for controlling flow separation and tested it with a NACA 0015 airfoil. Their PSJA produced a maximum velocity of 90 m/s at f = 130 Hz. The operation of the PSJAs markedly increased the angle of attack where the stall occurred from 12 degrees to 18 degrees. Additionally, the flow was visualized for both cases with and without PSJA actuation [28,29].

Another application of PSJA is in the fundamental studies of compressible turbulence. The conventional SJAs have been used to develop experimental facilities to generate isotropic turbulence with the interaction of many synthetic jets [30,31]. These experiments have been limited to low-Mach-number regimes, for which the assumption of incompressibility is valid. Recently, the PSJAs are used to generate turbulence under strong compressibility effects. Yamamoto *et al.,* developed a chamber facility, where opposing arrays of multiple PSJAs are used to generate nearly isotropic turbulence by the interaction of supersonic synthetic jets [32]. This facility was used to investigate the compressibility effects on statistical properties of turbulence [33].

In recent years, several experiments have been conducted to investigate the basic characteristics of PSJAs. These studies suggest that the PSJA performance is influenced by many independent parameters of the PSJA geometry that have to be determined in designing the PSJA. For example, the size of the cylinder, the stroke length and frequency of the piston, and the size of orifice holes have strong influences on the jet velocity. These influences have been investigated for conventional SJAs [34]. Due to the cost of building many different test models of PSJAs, experimental works may not

offer enough information on the PSJAs performance for different geometries. Moreover, the experiments can only offer limited information on velocity, pressure, and temperature distributions. Such a variety of information can be offered by numerical simulations. However, few previous studies have adapted the numerical simulations to investigate the flow induced by the PSJAs.

In this study, we perform large-eddy simulations (LESs) for PSJAs by OpenFOAM [35]. Here, the numerical model of the PSJA is developed based on the experiments by Sakakibara *et al.,* [36]. Because the experiment apparatus was successfully built in our laboratory, we first validate the numerical simulations by comparing the pressure inside the cylinder, which is one of the essential parameters of a PSJA, with the experimental results. The previous experiment has shown that the maximum pressure inside the cylinder is related to the maximum jet Mach number. This relationship is also verified by the simulation. Then, we investigate the jet flow generated by the PSJAs, which has not been investigated sufficiently in previous experimental studies. The paper is organized as follows. Section 2 explains numerical models. Section 3 discusses the fundamental characteristics of the PSJA. The conclusions are summed up in Section 4.

2. Numerical Procedures
2.1 Numerical Model of Piston Synthetic Jet Actuator

Figure 1 shows the schematic of the PSJA considered in this study. The numerical model is based on the PSJA developed in Sakakibara *et al.,* [36]. For simplicity, we consider the piston and cylinder with a square shape although the experiment used a round shape. However, the size of the actuator and the compression ratio are similar to the experiments, and the comparison between numerical simulations and experiments is meaningful. The actuator has a square orifice with a side length of d = 3 mm. As in Figure 1, when the piston is at the bottom dead center (BDC), the length of the cylinder is L_x = 21.7 mm. For the comparison with the experimental apparatus, the stroke length is L = 20.6 mm, which is the same as in the experiment. The distance from the top dead center (TDC) to the top of the cylinder is 1.1 mm. A point marked as P is the position where pressure and temperature histories are taken. Point P is located on the top surface of the cylinder and at the midpoint from the center of the orifice to the edge of the cylinder. This point is chosen because experiments of PSJA [36] install the pressure transducer near the orifice and measure the pressure on the top wall of the cylinder. The piston movement is described by a cosine function, which is explained in part C when the boundary conditions are presented. The frequency of the piston movement f is constant and is treated as a numerical condition.
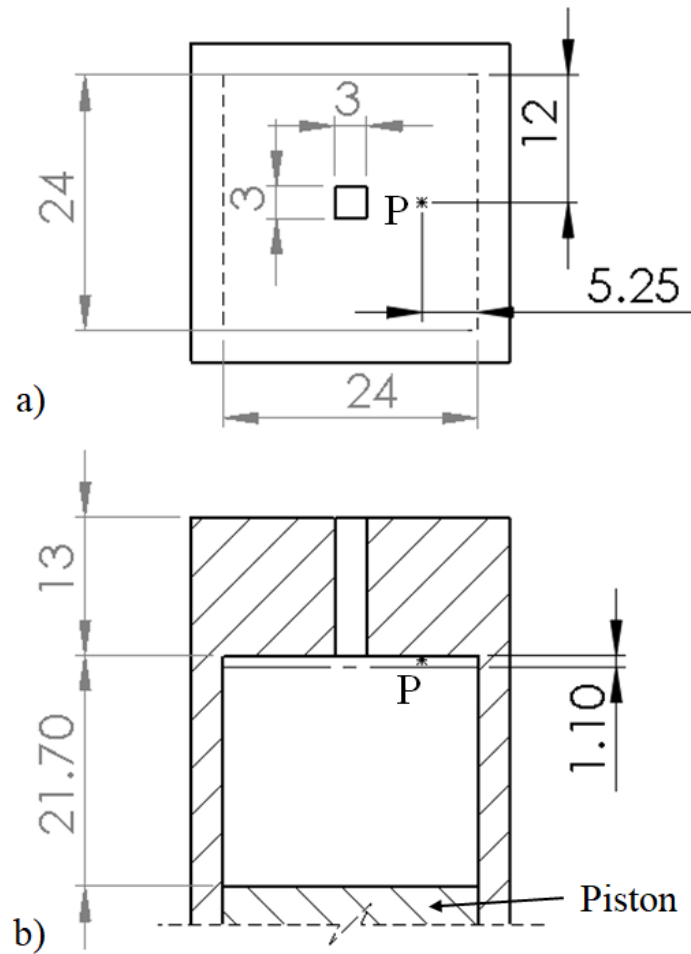
Fig. 1. A schematic of a piston synthetic jet actuator (PSJA):
a) top view; b) section front view. All dimensions are in mm

2.2 Numerical Methodology

We employ LES with the Smagorinsky model. The working fluid is assumed to be an ideal gas. The OpenFOAM software package is used in this study. The *rhoPimpleFoam*, which merges PISO (Pressure Implicit with Splitting of Operators [37]) and SIMPLE (Semi-Implicit Method for Pressure-Linked Equations [38]) algorithms, is utilized because the supersonic flow is induced by the PSJA and the fluid is significantly compressed or expanded in the cylinder. The solver is explained in detail by Holzmann [39]. The simulation employs the *backward time scheme* for time discretization, which is an implicit method with second-order accuracy. Spatial discretization is based on the *Gauss linear* scheme, which combines Gauss' theorem and the central difference scheme of second-order accuracy. Time step size is satisfied Courant criterion (with CFL < 0.1).

2.3 Computational Domain and Boundary Conditions

The simulations are performed with a computational domain shown in Figure 2a, which is composed of three domains, i.e., the piston/cylinder domain, the orifice domain, and the outflow domain, where the jet from the orifice is formed. All of the domains are rectangular and have sizes of (*Lx, Ly, Lz*) listed in Table 1. The origin of the coordinate (*x, y, z*) is set at the center of the orifice outlet.

The mesh is generated with the *blockMesh* utility. All domains use an orthogonal grid with a non-uniform grid spacing. As explained below, the cell size in the *x*-direction in the cylinder varies with time to deal with the piston movement. The non-uniform grid spacing is used in the outflow domain to provide better spatial resolution in the jet. Therefore, the cell size is larger near the lateral and the top boundaries of the outflow domain. The smallest cell size in the lateral direction is 0.5 mm, which is adapted to the centerline of the PSJA. From here, the lateral cell size expands at a ratio of 1.05 as it goes further from the center. The same procedure is used to determine the cell size in both *y* and *z* directions. By this method, the cell size in the *x*-direction is also increased from *x* = 0 as shown in Figure 2b, which shows the slice of the computational domain. The numbers of cells are determined by the above method and the geometrical dimensions, which are summarized in Table 1. For reference, Figure 2c illustrates the grid distribution in the region of interest, where the jet flow is formed.

The bottom wall of the cylinder part is the top surface of the piston. Therefore, the bottom boundary location and the cell size in the cylinder part vary with time. This function is coded with *dynamicInkJetFvMesh* class of OpenFOAM. The velocity of the piston reaches the absolute peak values at the half stroke length in each cycle, then approaches zero at TDC or BDC. Figure 3a shows the mesh distribution when the piston is either at the BDC or the TDC. The piston position x_P is given explicitly by a cosine function as

$$x_p = x_c + \frac{1}{2}L\cos(2\pi f t + \omega_0), \tag{1}$$

where the center location of the piston movement is $x_c = -24.4$ mm, *t* is the time, and $\omega_0 = \pi$ is the initial phase. Figure 3b shows the piston velocity U_p given by the time derivative of x_P. Here, *t* is normalized by a period of one cycle *T* = 1/*f*. As the piston moves, the size of the piston/cylinder domain changes. The mesh distribution is adjusted based on the piston position while the number of the cells is unchanged during the simulations.

For the outflow domain (Figure 2a), all the computational boundaries except for the surface with the orifice are treated with the *waveTransmissive* boundary condition, which is a non-reflecting boundary condition. The slip condition is applied to the internal surface of the orifice and the cylinder surface because the region of interest is an outflow from the orifice and the boundary layers on these surfaces are not objects to observe. The piston top is the boundary moving at a velocity given by Eq. (1). This boundary condition is realized with the *movingWallVelocity,* which is a class built in OpenFOAM code.

The same initial condition is adapted in the entire domain. The initial pressure is the atmospheric pressure P_{atm} = 101,325 Pa and temperature T_0 is 300 K. The initial velocity is zero for three components of velocity vectors. The simulation is conducted for *f* = 50, 75, 100, 125, and 150 Hz*.* For each case, time is advanced over 6*T*. For the case of *f* = 100 Hz, the simulation is conducted over 20*T* for the calculation of velocity statistics of the jet. The results presented in this paper are taken after the fourth cycle to eliminate the transient behaviour from the initial state.

Table 1
The domain sizes and the numbers of cells

Domain	Size (mm)	Number of cells
	(*Lx, Ly, Lz*)	(*Nx, Ny, Nz*)
Piston/Cylinder	(21.7, 24, 24)	(24, 36, 36)
Orifice	(13, 3, 3)	(26, 6, 6)
Outflow domain	(360, 483, 483)	(74, 138, 138)
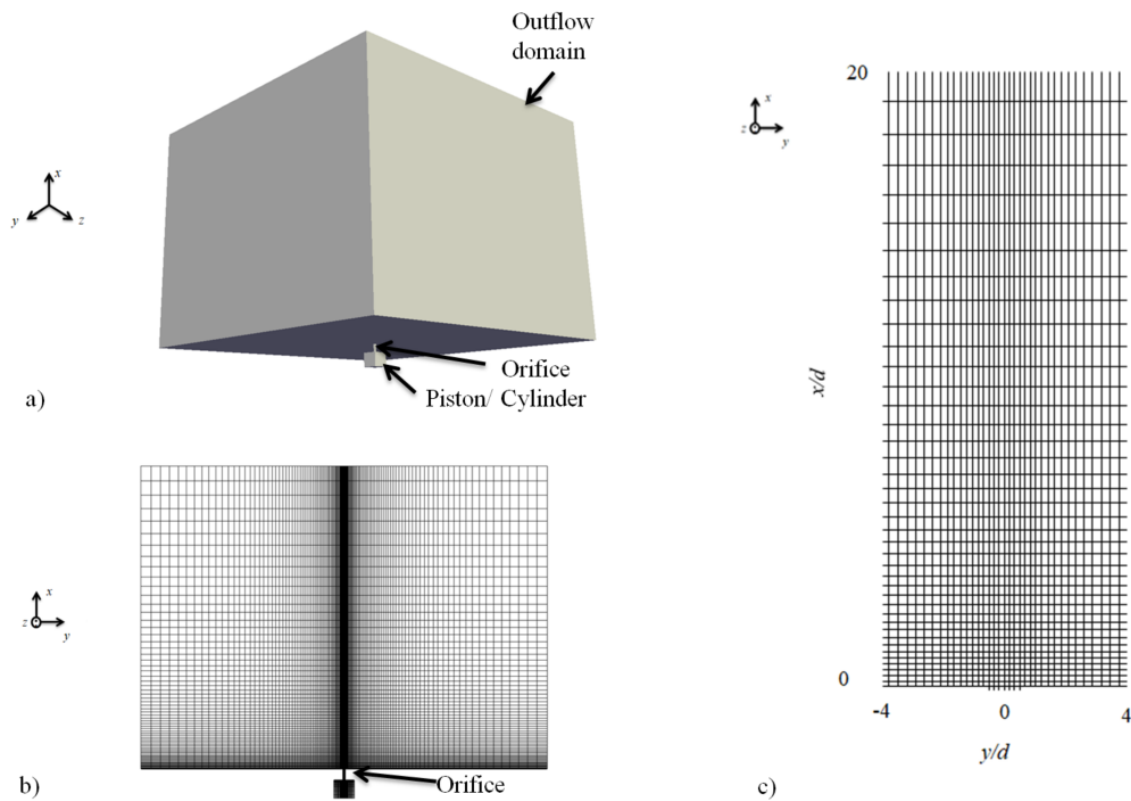
Fig. 2. The computational domain and the grid: a) the overall view of the computational domain; b) grid distribution on the center plane of the computational domain; c) the grid near the orifice area
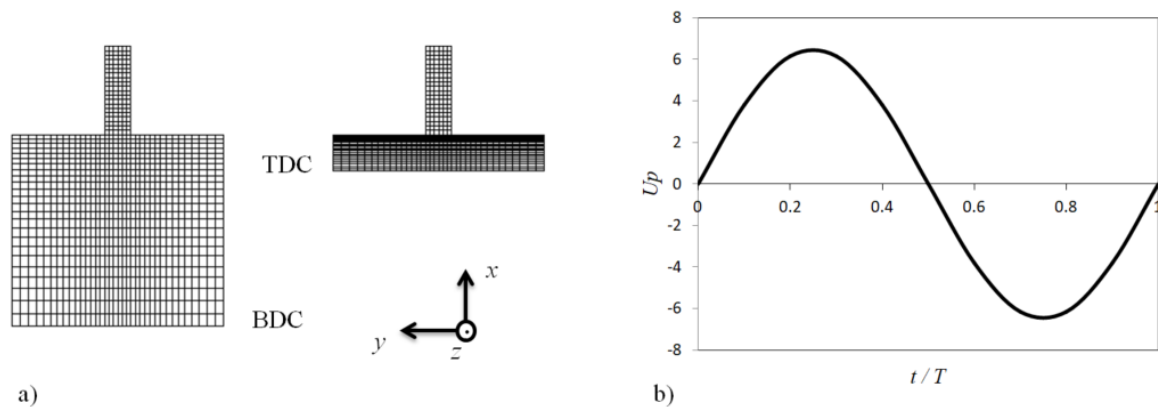
Fig. 3. a) Grid distribution when the piston is located at TDC or BDC and b) time history of piston velocity

2.4 Grid Independence Test

A grid independence test is conducted for the simulation case of 100 Hz. An additional simulation for this test uses a smaller number of cells than the main simulations as summarized in Table 2.

Table 2
The domain sizes and the number of cells for the test case

Domain	Size (mm) (*Lx, Ly, Lz*)	Number of cells (*Nx, Ny, Nz*)
Piston/Cylinder	(21.7, 24, 24)	(15, 21, 21)
Orifice	(13, 3, 3)	(13, 3, 3)
Outflow domain	(360, 483, 483)	(60, 111, 111)

We compare the pressure histories at point P inside the cylinder in Figure 4. The position of point P is shown in Figure 1a. Time t is normalized by the period of one cycle T while P_r is the absolute pressure P normalized by P_{atm}, $P_r = P/P_{atm}$. As also discussed in Sec. 3, the pressure increases and decreases by the compression and expansion of the fluid caused by the piston movement, respectively, and the pressure is related to the jet velocity at the orifice exit. The pressure waveform is also related to the intermittent behaviour of the synthetic jet because the blowing and suction phases approximately correspond to times of $P_r > 1$ and $P_r < 0$. The results show only slight differences between the two cases with different resolutions, suggesting that the jet behaviour is not influenced by the resolution.
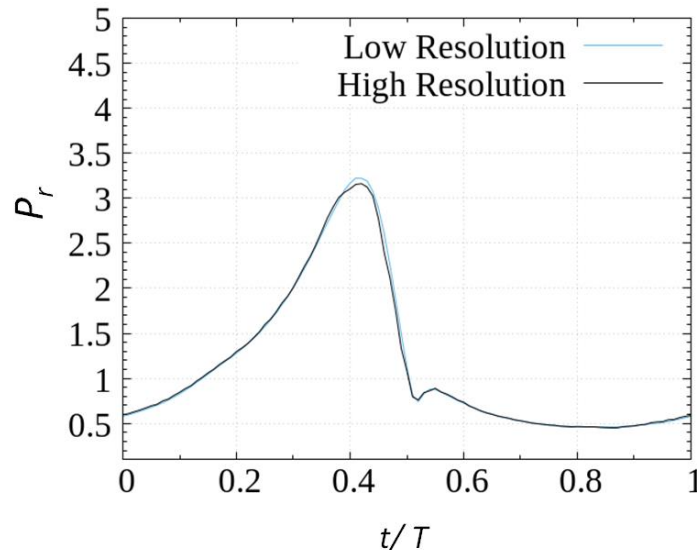
Fig. 4. Comparison of normalized pressure P_r for $0 \leq t/T \leq 1$ between two cases with different resolutions. Both simulations are conducted for f = 100 Hz

3. Results

3.1 Time Histories of Pressure Inside the Cylinder

The pressure inside the cylinder is related to the jet velocity [36]. The time-series data of pressure is taken at point P on the internal surface of the cylinder (Figure 1). Figure 5 compares the absolute pressure P normalized by P_{atm}, $P_r = P/P_{atm}$, in two cycles for f = 50, 75, 100, and 150 Hz. At time t/T = 0 and 1, the piston is at the BDC. It is confirmed that the difference in the pressure between the two cycles is small.

The frequency dependence of P_r is shown in Figure 6. A peak pressure can be reached later in terms of time (t_{peak}/T) for a higher frequency. The values of t_{peak}/T are 0.345, 0.383, 0.410, and 0.433 for f = 50, 75, 100, and 150 Hz, respectively: As f increases, they are shifted toward the time t/T = 0.5 at which the piston locates at the TDC. The pressure histories are distinctly asymmetric as also reported in experiments [36].

Figure 7 shows a comparison of the pressure history between the simulation and the experimental results of the PSJA with a single round orifice with a diameter d = 3 mm [36]. Although the orifice shapes are different between the simulation and the experiment, their compression ratio and the ratio (S_1/S_2) between the cross-sections of the cylinder (S_1) and the orifice (S_2) are the same. Here, the results are plotted against (t - t_{peak})/T for comparison with experiments, in which the piston position was not measured. In this figure, we compare the pressure histories of three cases with f = 50, 75, and 100 Hz for both experiments and simulations while the simulation data of f = 150 Hz is also shown as a reference. The maximum and minimum pressures increase and decrease, respectively, as f increases. The pressure histories are consistent between the simulations and the experiments even though different shapes of the orifice are utilized.

Figure 8 presents the frequency dependence of the maximum and minimum pressures, P_{rmax} and P_{rmin}, compared with the experiments [36]. The f dependence of P_{rmax} and P_{rmin} agrees well with the experiments. A flow inside an orifice hole is expected to be sonic when $P_r \geq 1.893$ and $P_r \leq 0.528$ in the blowing phase and suction phase, respectively [40]. These conditions are shown with horizontal broken lines. The results of the simulation and the experiment suggest that both conditions are satisfied for f > 100 Hz. However, the flow in the blowing phase can be sonic when the frequency exceeds about 60 Hz.
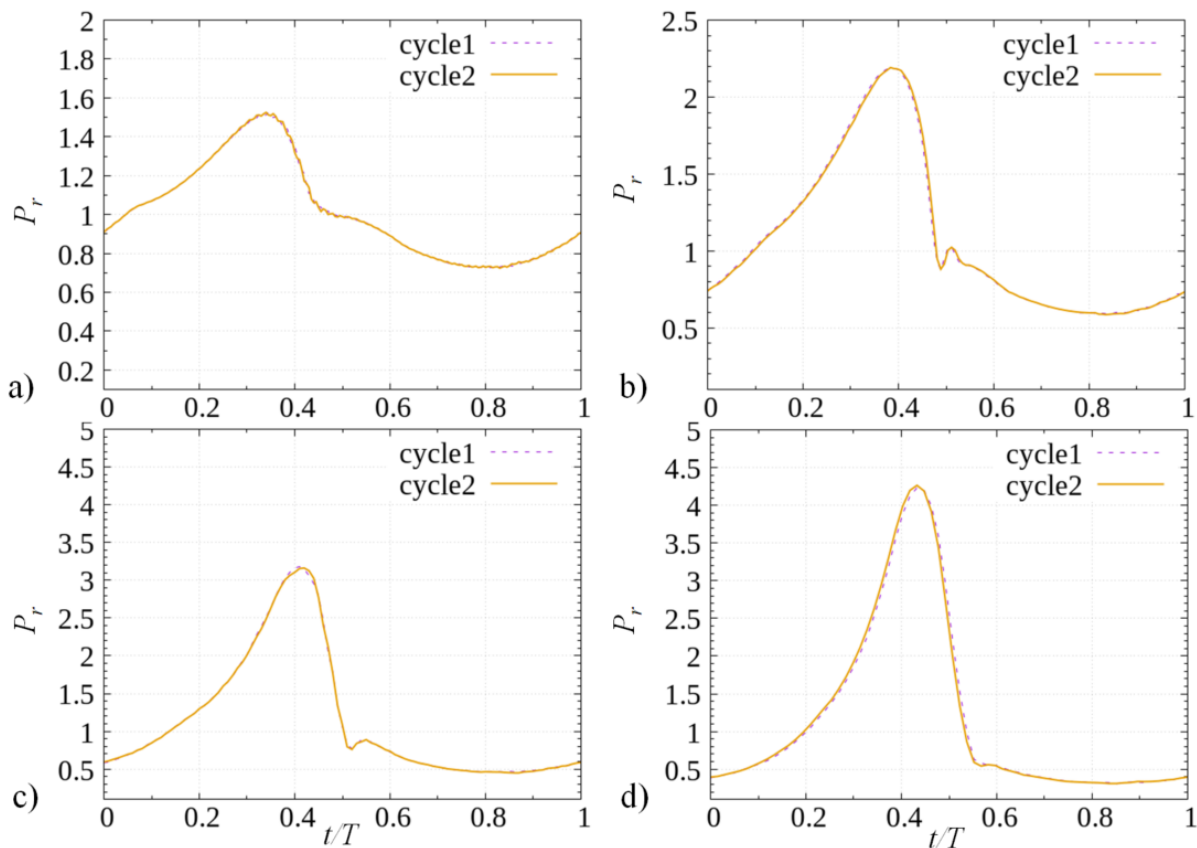
Fig. 5. Comparison of normalized pressure *Pr* for 0 ≤ *t/T* ≤ 1 between two different cycles: a) *f* = 50 Hz; b) *f* = 75 Hz; c) *f* = 100 Hz; d) *f* = 150 Hz
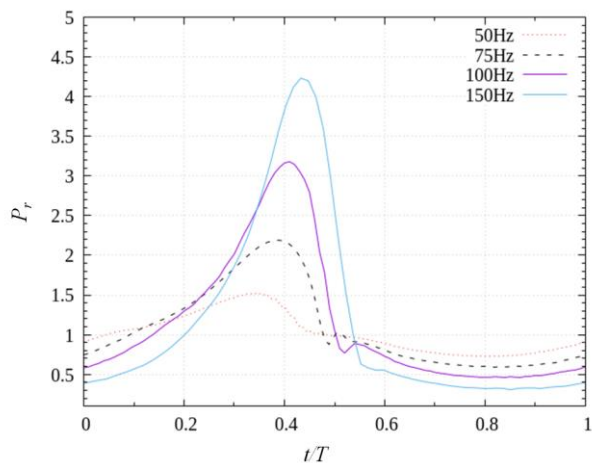
Fig. 6. Time histories of normalized pressure with different frequencies
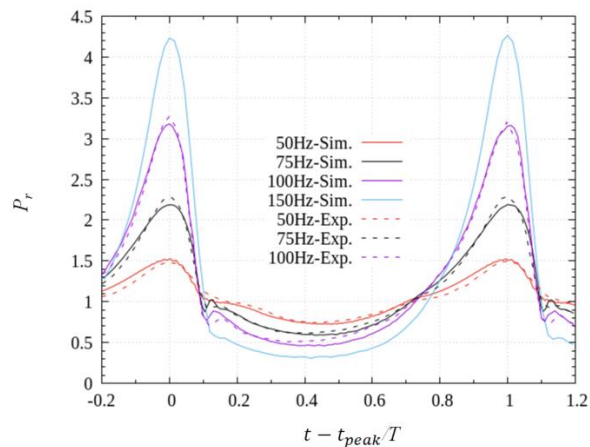
Fig. 7. Comparison of normalized pressure between the simulation (Sim.) and experiment (Exp.)
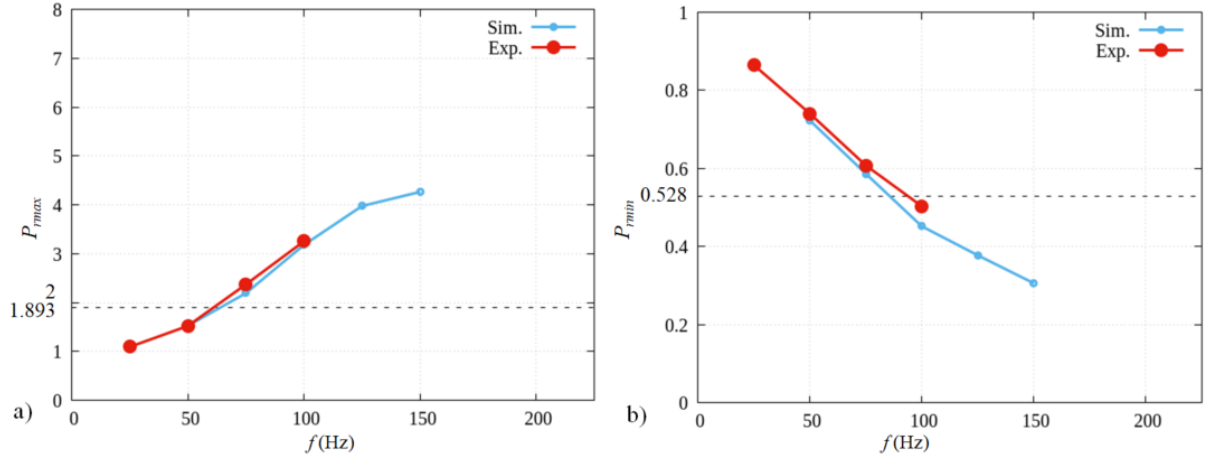
Fig. 8. a) Maximum and b) minimum normalized pressure for different frequencies

3.2 Mach Number History

Figure 9 shows the Mach number $M = |u|/a$ of the flow at the orifice exit as a function of time, where u is the exit velocity and a is the local speed of sound. The Mach number becomes close to zero and attains a local minimum when the flow direction at the orifice exits changes between blowing and suction phases, which can be roughly identified as time with $t/T < 0.5$ and $t/T > 0.5$, respectively. The small non-zero values observed between the suction and blowing phases are mostly due to the time lag between the piston movement and fluid motion. The non-zero velocity in the y and z directions could also have a small effect on this. The time to reach the maximum value is not at the middle of the half-cycle when the piston speed is maximum (t/T= 0.25), but it is delayed as the frequencies increase. This trend agrees with the time of the maximum pressure in the cylinder shown in Figure 5. The maximum Mach number is achieved at t/T = 0.340, 0.383, 0.430, and 0.429, respectively, for f = 50, 75, 100, and 150 Hz, and they are close to times at which the pressure reaches the maximum. The time of the first minimum value of M, M_{min}, also increases: t/T = 0.06, 0.11, 0.15, and 0.21 with the corresponding frequency values of f = 50, 75, 100, and 150 Hz. These times are roughly corresponding to those when $P_r = 1$ shown in Figure 6. These results suggest the correlation between M and P_r. Immediately after reaching the maximum Mach number, M_{max}, the Mach number decreases very sharply also as in the trend of P_r.

The value of Mach number M_{is} of an isentropic flow through a Laval nozzle is calculated as [32]:

$$\frac{p_0}{p} = \left(1 + \frac{\gamma-1}{2}M_{is}^2\right)^{\frac{\gamma}{\gamma-1}}, \tag{2}$$

where p_0 is the stagnation pressure, p is the pressure at M_{is}, and γ = 1.4 is the specific heat ratio. From Eq. (2), we expect the following relation between M_{max} and P_{rmax}:

$$M_{max} = \left\{\frac{2}{\gamma-1}\left(P_{rmax}^{\frac{\gamma-1}{\gamma}} - 1\right)\right\}^{\frac{1}{2}}. \tag{3}$$

Figure 10 shows M_{max} as a function of P_{rmax}. As expected, M_{max} increases with P_{rmax}. The simulation results are pretty close to the theoretical results, and Eq. (3) is useful for estimating the maximum Mach number from the pressure in the cylinder. However, the experimental results of Sakakibara *et al.,* [36] suggest that the actual Mach number is slightly lower than Eq. (3). Since the slip boundary

condition is applied in the orifice, this difference suggests that the viscous effects in the orifice reduce the jet Mach number.
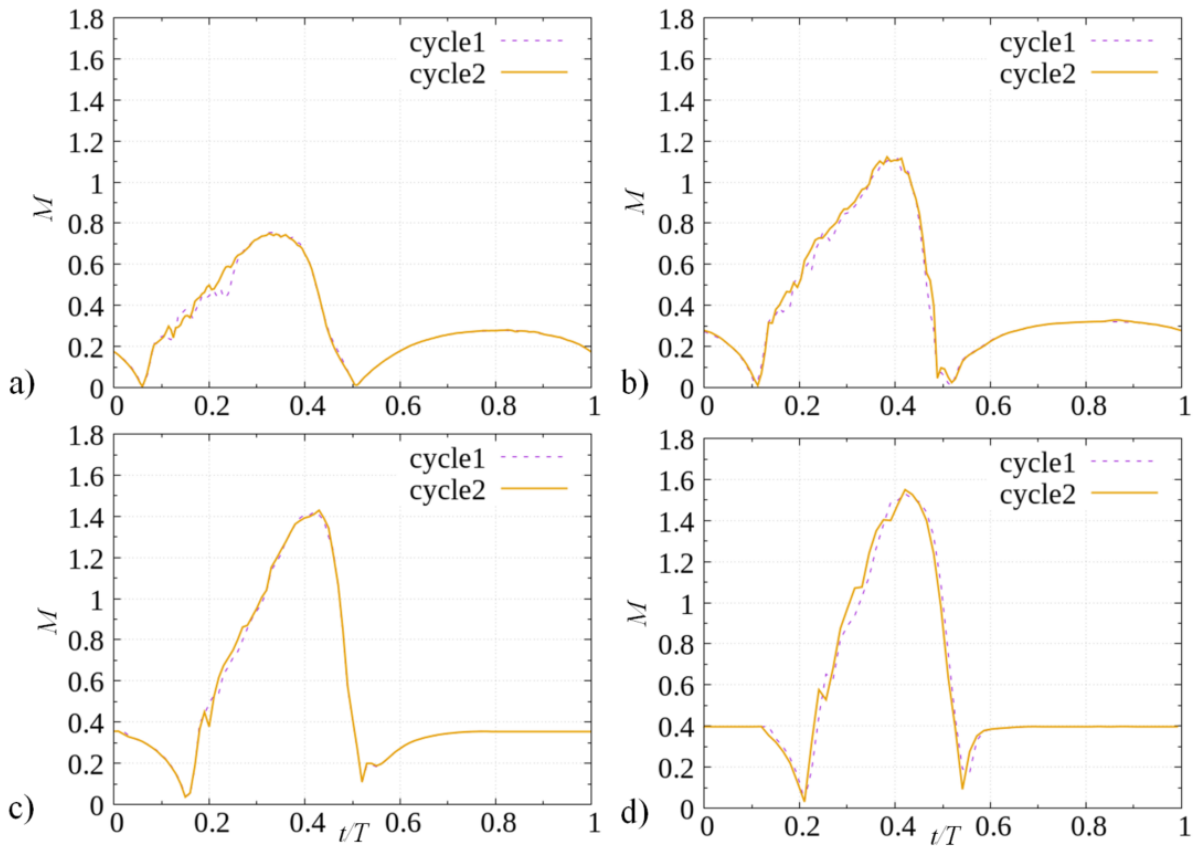
Fig. 9. Time histories of Mach number at the orifice exit for different frequencies: a) f = 50 Hz; b) f = 75 Hz; c) f = 100 Hz; d) f = 150 Hz
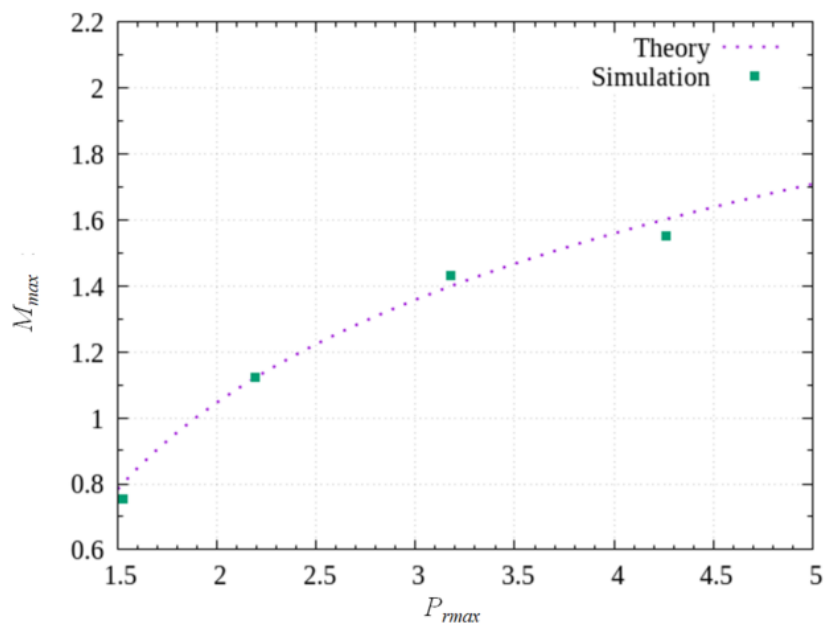
Fig. 10. Relationship between the maximum pressure and the maximum Mach number for f = 50, 75, 100, and 150 Hz

3.3 Time Histories of Temperature inside the Cylinder

Figure 11 shows the time histories of the temperature inside the cylinder at point P, where the cylinder pressure is also taken in Figures 5-7. Here, the temperature T normalized by the ambient temperature T_0, $T_r = T/T_0$, is shown for two consecutive cycles. The trend of temperature is quite similar to that of pressure because an increase in frequency leads to large variations of pressure and gas temperature, which are linked with the equation of state. The shorter time between the suction phase and the flowing phase of the piston's movement may lead to this more considerable variation. The result is also qualitatively consistent with the simulation of Crittenden *et al.,* [24], who describe the increasing gas temperature with an increase in frequency. Here, the maximum temperature values are 364, 425, 592, and 802 K for f = 50, 75, 100, and 150 Hz, respectively. This temperature increase inside the cylinder can be important in the experimental investigation of the PSJA. Yamamoto *et al.,* [33] conducted velocity measurement of turbulence generated by the PSJAs by seeding tracer particles of particle image velocimetry with engine oil evaporated by the temperature variation inside the cylinder. The present result suggests that this seeding method requires a large temperature variation at a high frequency.
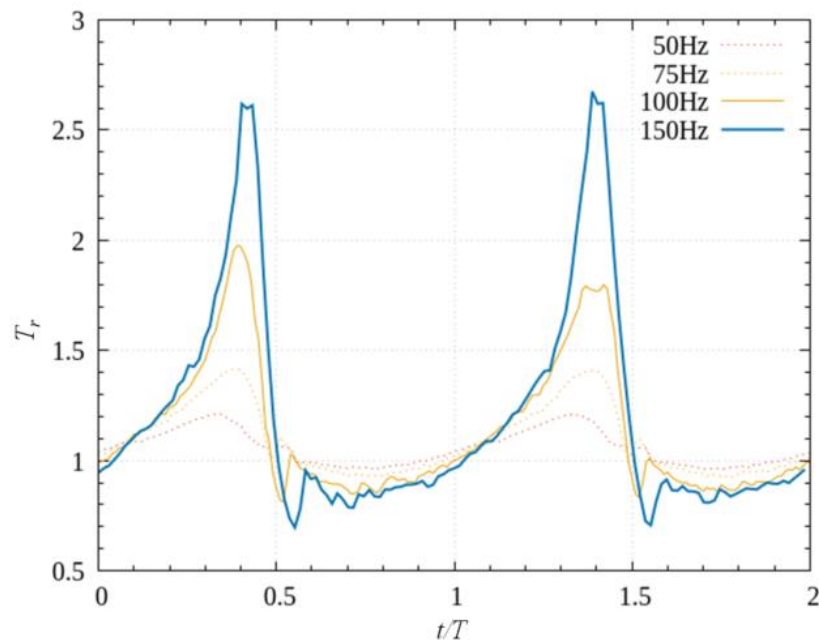
Fig. 11. Time histories of the temperature inside the cylinder for
f = 50, 75, 100, and 150 Hz

3.4 Reynolds Number History

Figure 12 shows the variations of the jet Reynolds number (*Re*) at the orifice exit with different frequencies. Here, *Re* is defined as

$$Re = \frac{\rho V D}{\mu}, \tag{4}$$

where ρ is the density, V is the velocity at the orifice exit, D is the sidelength of the orifice, and μ is the viscosity coefficient. *Re* is evaluated at (y, z) = (0, 0). In the blowing phase, *Re* reaches about 50000 even for the lowest-frequency case. Therefore, the jet issued from the orifice becomes

turbulent. The highest *Re* in one cycle increases with the frequency *f*; the corresponding maximum Re are 49445, 70218, 83297, and 83682 for 50, 75, 100, and 150 Hz, respectively. The times for reaching these maximum values are accompanied by the changing of pressure in the flowing phases in Figure 6. The maximum Re increases more slowly with *f* at higher *f*. This tendency agrees with the *f* dependence of the maximum Mach number in Figure 9. Therefore, the behavior of the jet shows a weaker dependence on *f* when *f* is large enough.
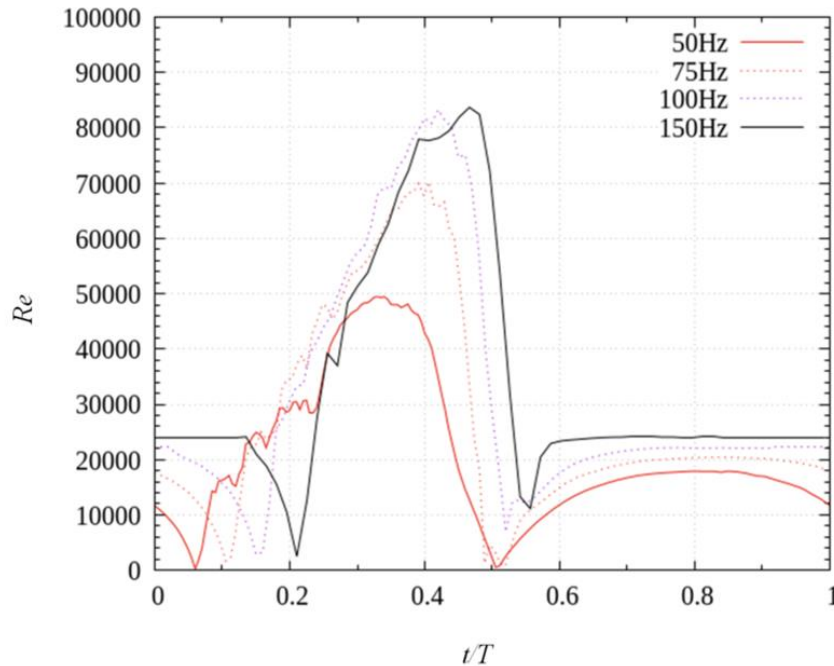
Fig. 12. Time histories of Reynold numbers with different frequencies

3.5 Phase-Averaged Flow-field

The jet is periodically issued from the orifice hole. Therefore, the velocity field in the jet is investigated with a phase average, conditioned on the piston position x_p, which is directly related to time by Eq. (1). Figure 13 visualizes the flow field of the jet with the color contour of the phase-averaged velocity in the *x*-direction *U* for *f* = 100 Hz, while Figure 14 plots *U* along the jet centerline from the orifice hole. In these figures, time is advanced from (a) to (j) with an increment of 0.1*T*. At *t/T* = 0.1 (Figures 13a and 14a), the flow is in the suction phase with the flow direction toward the cylinder (*U* < 0), even though the piston is moving toward the TDC. However, by the time *t/T* = 0.2 (Figures 13b and 14b), the velocity profile has changed significantly and the jet is strongly issued outward from the orifice. At *t/T* = 0.2, the velocity de-escalates in the *x*-direction at around *x/d* = 4– 6 indicating that the jet has reached this position. After this time, the jet velocity increases substantially and the velocity at the orifice exit reaches the maximum approximately at *t/T* = 0.4 (Figures 13d and 14d). Following this, the velocity is gradually reduced and transitions to the suction phase. In the suction phase, the velocity toward the orifice is observed around the orifice exit. However, the flow that is induced in the suction phase does not extend far from the orifice: *U* is close to 0 for *x/d* >2 in Figures 14(f-j). The present results from 0.3*T* to 0.5*T* are qualitatively consistent with the measurements with particle image velocimetry [24]. They reported that the shock cells appear inside the jet near the orifice when the jet velocity becomes large. The appearance of the shock cell is also confirmed as the velocity oscillation near the jet exit (0 < *x/d* < 2) although the shock structures are not accurately captured by large-eddy simulations because of the spatial resolution.

In Figure 15, we plot the root-mean-square (rms) of velocity fluctuations in the *x*-direction at a given phase, U_{rms}, along the centreline from the orifice from *t/T* = 0.1 to 1 with a time increment of 0.1*T*. Here, U_{rms} is calculated from 20 snapshots of 20 consecutive piston cycles using the phase average. Through this figure, high turbulence level occurs in Figures 15 (b-d) corresponding to *t/T* = 0.2-0.4. At *t/T* = 0.2, the jet has reached *x/d* = 4-6 (Figure 14b), where the velocity fluctuations are large, and the tip of the jet has strong turbulent fluctuations. Turbulence level is particularly high at a position far from the orifice in the range *x/d* >10 at *t/T* = 0.3 and 0.4, respectively. At *t/T* = 0.5 when the piston is at TDC, U_{rms} has a peak in the near field (Figure 15e). This period corresponds to the time when P_r considerably drops as shown in Figure 6. Therefore, the large U_{rms} in the near field at this time may be due to the strong deceleration of the jet. The turbulence level in the suction phase (Figures 15(f-j)) is much lower than in the blowing phase. Velocity fluctuations are produced by a mean velocity gradient in a turbulent jet, where both mean velocity gradient and rms of velocity fluctuations are large off the jet centerline [41,42]. The large transverse gradient of *U*, $\partial U/\partial y$ (and also $\partial U/\partial z$ due to the symmetry), in Figure 13(b-d) can cause large velocity fluctuations in the blowing phase. However, the mean velocity gradient is small in the suction phase in Figures 13(f-j), and the production of turbulence hardly occurs in the suction phase.
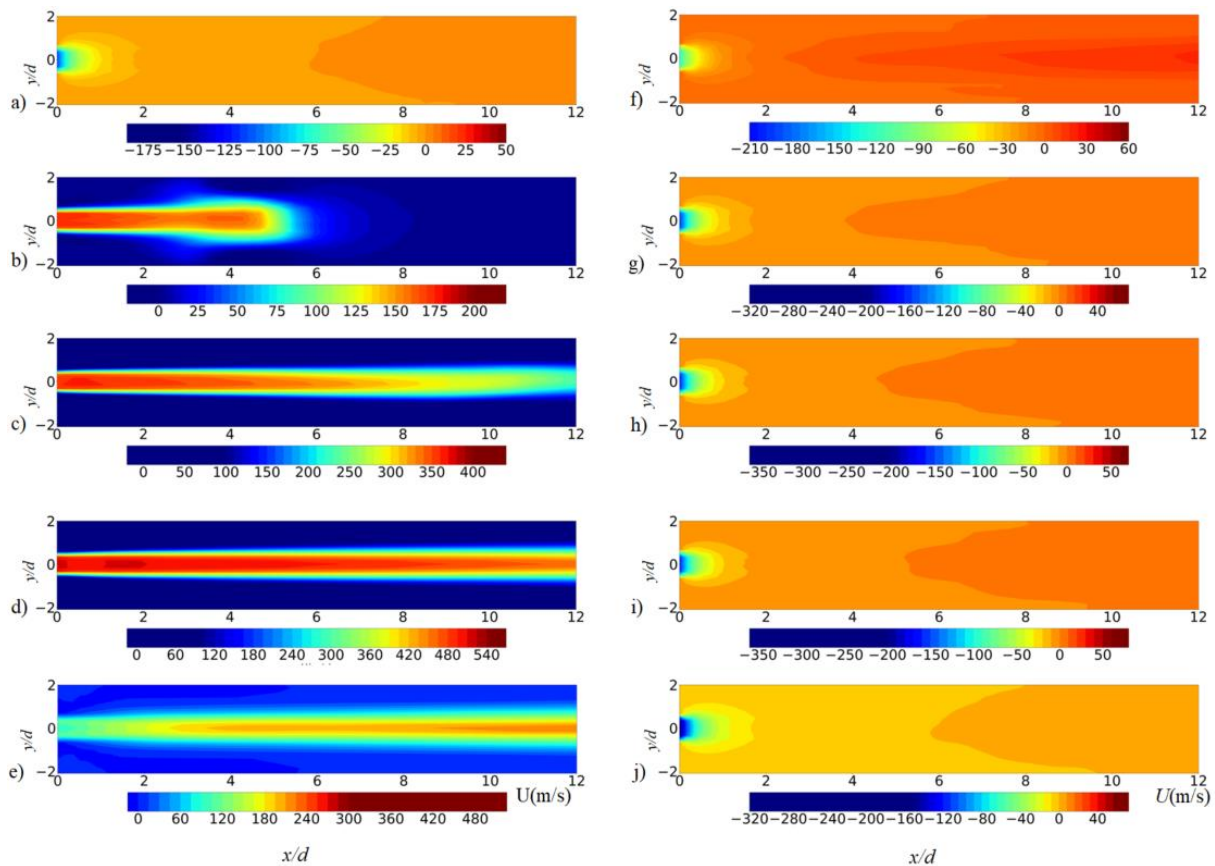
Fig. 13. Phase-averaged velocity in the *x*-direction for *f* = 100 Hz at a) *t/T* = 0.1, b) 0.2, c) 0.3, d) 0.4, e) 0.5, f) 0.6, g) 0.7, h) 0.8, i) 0.9, and j) 1.0
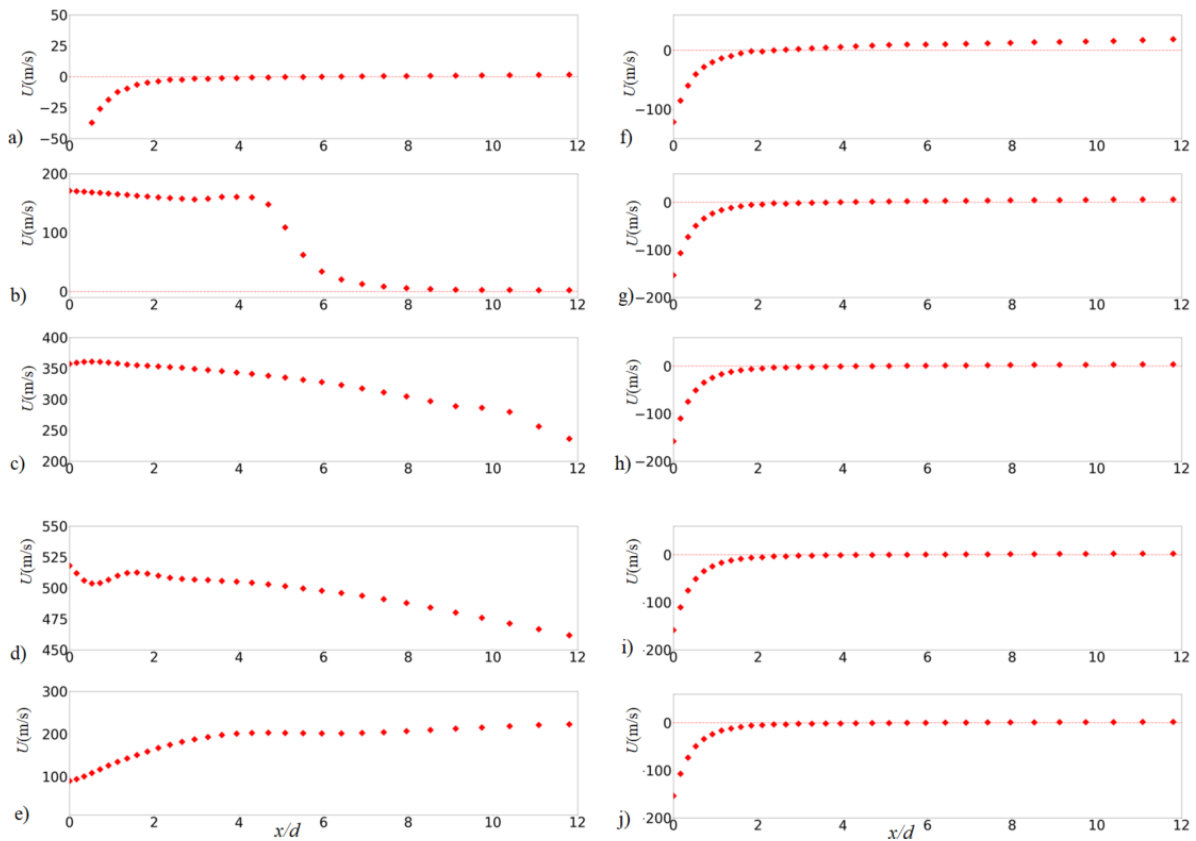
Fig. 14. Phase-averaged velocity in the x-direction along the centerline for f = 100 Hz, at a) t/T = 0.1, b) 0.2, c) 0.3, d) 0.4, e) 0.5, f) 0.6, g) 0.7, h) 0.8, i) 0.9, and j) 1.0
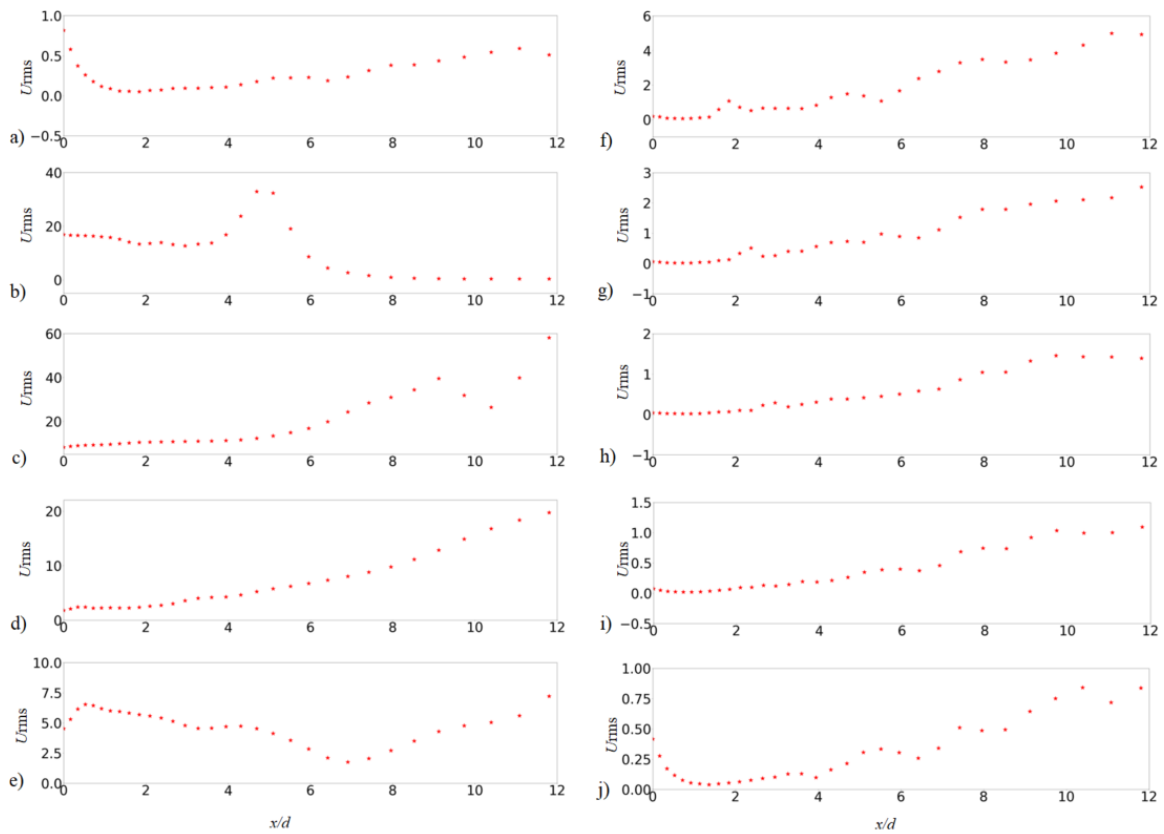
Fig. 15. Rms fluctuations of velocity in the *x*-direction, *U*rms, along the centerline for f = 100 Hz, at a) t/T = 0.1, b) 0.2, c) 0.3, d) 0.4, e) 0.5, f) 0.6, g) 0.7, h) 0.8, i) 0.9, and j) 1.0

4. Conclusions

We investigated the properties of a compressible flow generated by a PSJA with a square orifice by employing LESs using OpenFOAM. The LES was validated by comparing the time histories of pressure inside the cylinder with previous experiments with a similar model geometry of the PSJA. It is demonstrated that the present numerical schemes employed with OpenFOAM are useful for investigating the flow induced by PSJAs with numerical simulations, which will be important in the future investigation of the PSJAs with various geometries.

The pressure inside the cylinder and jet Mach number at the orifice exit hardly fluctuate among different cycles of the piston movement, and the characteristics of the jets are statistically identical for all cycles. The maximum and minimum pressures become larger and lower with increasing f, respectively. The maximum Mach number is well represented as a function of the maximum pressure, and their relation is consistent with the theoretical estimation. The pressure variation in the cylinder also results in temperature variations. We also found that the maximum temperature inside the cylinder exceeds 800 K when the piston frequency is 150 Hz. With this frequency, the jet Reynolds number, Re, at the orifice exit can reach about 0.83×10^6. As also confirmed for the Mach number, Re increases with the frequency f although the frequency dependence becomes weaker for higher f.

The analysis of the phased-averaged velocity field suggests that the suction and blowing phases do not perfectly match with the downward and upward movements of the piston, respectively. Similarly, the time at which the cylinder pressure reaches the maximum does not coincide with the time of the maximum Mach number. The rms velocity fluctuations U_{rms} are large in the region where the flow is decelerated at the furthest location of the jet. The large U_{rms} in the near field is also related to the strong deceleration of the jet. When the Mach number becomes the maximum value, the turbulence level becomes high at the far-field. The velocity fluctuations are small in the suction phase because of small mean velocity gradients in the jet transverse direction.

References
[1] Lin, John C. "Review of research on low-profile vortex generators to control boundary-layer separation." *Progress in Aerospace Sciences* 38, no. 4-5 (2002): 389-420. https://doi.org/10.1016/S0376-0421(02)00010-6
[2] Gao, Linyue, Hui Zhang, Yongqian Liu, and Shuang Han. "Effects of vortex generators on a blunt trailing-edge airfoil for wind turbines." *Renewable Energy* 76 (2015): 303-311. https://doi.org/10.1016/j.renene.2014.11.043
[3] Bragg, M. B., and G. M. Gregorek. "Experimental study of airfoil performance with vortex generators." *Journal of aircraft* 24, no. 5 (1987): 305-309. https://doi.org/10.2514/3.45445
[4] Cattafesta III, Louis N., and Mark Sheplak. "Actuators for active flow control." *Annual Review of Fluid Mechanics* 43 (2011): 247-272. https://doi.org/10.1146/annurev-fluid-122109-160634
[5] Lee, Chester, Guang Hong, Q. P. Ha, and S. G. Mallinson. "A piezoelectrically actuated micro synthetic jet for active flow control." *Sensors and Actuators A: Physical* 108, no. 1-3 (2003): 168-174. https://doi.org/10.1016/S0924-4247(03)00267-X
[6] Smith, Barton L., and Ari Glezer. "The formation and evolution of synthetic jets." *Physics of fluids* 10, no. 9 (1998): 2281-2297. https://doi.org/10.1063/1.869828
[7] Glezer, Ari, and Michael Amitay. "Synthetic jets." *Annual review of fluid mechanics* 34, no. 1 (2002): 503-529. https://doi.org/10.1146/annurev.fluid.34.090501.094913
[8] Ariffin, Ahmad Hamdan, and Kamarul Ariffin Ahmad. "Computational Fluid Dynamic (CFD) Simulation of Synthetic Jet Cooling: A Review." *Journal of Advanced Research in Fluid Mechanics and Thermal Sciences* 72, no. 2 (2020): 103-112. https://doi.org/10.37934/arfmts.72.2.103112

[9]   Husin, Azmi, Mohd Zulkifly Abdullah, Azmi Ismail, Ayub Ahmed Janvekar, Mohd Syakirin Rusdi, and Wan Mohd Amri Wan Mamat Ali. "Heat Transfer Performance of a Synthetic Jet Generated by Diffuser-Shaped Orifice." *Journal of Advanced Research in Fluid Mechanics and Thermal Sciences* 53, no. 1 (2019): 122-128.

[10]   Amitay, Michael, Andrew Honohan, Mark Trautman, Ari Glezer, Michael Amitay, Andrew Honohan, Mark Trautman, and Ari Glezer. "Modification of the aerodynamic characteristics of bluff bodies using fluidic actuators." In *28th Fluid Dynamics Conference*, p. 2004. 1997. https://doi.org/10.2514/6.1997-2004

[11]   Crook, Andrew, Amit Sadri, and Norman Wood. "The development and implementation of synthetic jets for the control of separated flow." In *17th Applied Aerodynamics Conference*, p. 3176. 1999. https://doi.org/10.2514/6.1999-3176

[12]   Chen, Y., S. Liang, K. Aung, A. Glezer, and J. Jagoda. "Enhanced mixing in a simulated combustor using synthetic jet actuators." In *37th aerospace sciences meeting and exhibit*, p. 449. 1999. https://doi.org/10.2514/6.1999-449

[13]   Lyubimov, D. A., and I. V. Potekhina. "Application of the RANS/ILES method in analyzing the efficiency of the control of separation flows in diffusers using synthetic jets." *Fluid Dynamics* 50 (2015): 590-599. https://doi.org/10.1134/S0015462815040146

[14]   Sato, Makoto, Koichi Okada, Kengo Asada, Hikaru Aono, Taku Nonomura, and Kozo Fujii. "Unified mechanisms for separation control around airfoil using plasma actuator with burst actuation over Reynolds number range of 103–106." *Physics of Fluids* 32, no. 2 (2020): 025102. https://doi.org/10.1063/1.5136072

[15]   Keisar, David, David Hasin, and David Greenblatt. "Plasma actuator application on a full-scale aircraft tail." *AIAA Journal* 57, no. 2 (2019): 616-627. https://doi.org/10.2514/1.J057233

[16]   Zainuddin, Farah Ayiesya, and Nazri Md Daud. "A review on dielectric barrier discharge (dbd) plasma actuator in aeronautics applications." *Journal of Advanced Research in Fluid Mechanics and Thermal Sciences* 48, no. 2 (2018): 125-132.

[17]   Santhanakrishnan, Arvind, and Jamey D. Jacob. "Flow control with plasma synthetic jet actuators." *Journal of Physics D: Applied Physics* 40, no. 3 (2007): 637. https://doi.org/10.1088/0022-3727/40/3/S02

[18]   Thomas, Flint O., Thomas C. Corke, Muhammad Iqbal, Alexey Kozlov, and David Schatzman. "Optimization of dielectric barrier discharge plasma actuators for active aerodynamic flow control." *AIAA journal* 47, no. 9 (2009): 2169-2178. https://doi.org/10.2514/1.41588

[19]   Jolibois, J., and E. Moreau. "Enhancement of the electromechanical performances of a single dielectric barrier discharge actuator." *IEEE Transactions on Dielectrics and Electrical Insulation* 16, no. 3 (2009): 758-767. https://doi.org/10.1109/TDEI.2009.5128516

[20]   Dahalan, Md Nizam, Hafizah Zahari, Ainullotfi Abdul-Latif, Shabudin Mat, Shuhaimi Mansor, Norazila Othman, Mastura Abd Wahid et al. "Feasibility Study of Plasma Actuator for Flow Separation Control." *Journal of Advanced Research in Fluid Mechanics and Thermal Sciences* 65, no. 2 (2020): 201-212.

[21]   Vernet, Julie A., Ramis Örlü, and P. Henrik Alfredsson. "Flow separation control by dielectric barrier discharge plasma actuation via pulsed momentum injection." *AIP Advances* 8, no. 7 (2018): 075229. https://doi.org/10.1063/1.5037770

[22]   Moreau, E., Jonathan Cazour, and N. Benard. "Influence of the air-exposed active electrode shape on the electrical, optical and mechanical characteristics of a surface dielectric barrier discharge plasma actuator." *Journal of Electrostatics* 93 (2018): 146-153. https://doi.org/10.1016/j.elstat.2018.04.005

[23]   Ebrahimi, Abbas, Majid Hajipour, and Kamran Ghamkhar. "Experimental study of stall control over an airfoil with dual excitation of separated shear layers." *Aerospace Science and Technology* 82 (2018): 402-411. https://doi.org/10.1016/j.ast.2018.09.027

[24]   Crittenden, Thomas M., and Ari Glezer. "A high-speed, compressible synthetic jet." *Physics of Fluids* 18, no. 1 (2006): 017107. https://doi.org/10.1063/1.2166451

[25]   Traub, Lance W., Michael Sweet, and Karl Nilssen. "Evaluation and characterization of a lateral synthetic jet actuator." *Journal of aircraft* 49, no. 4 (2012): 1039-1050. https://doi.org/10.2514/1.C031545

[26]   Eri, Qitai, Liang Hong, and Ting Li. "Novel Piston-Type Synthetic Jet Actuator with Auxiliary Air Inlet." *Journal of Aerospace Engineering* 32, no. 1 (2019): 04018127. https://doi.org/10.1061/(ASCE)AS.1943-5525.0000936

[27]   Gilarranz, J. L., L. W. Traub, and O. K. Rediniotis. "Characterization of a compact, high-power synthetic jet actuator for flow separation control." In *AIAA Aerospace Sciences Meeting & Exhibit, 40 th, Reno, NV*. 2002. https://doi.org/10.2514/6.2001-737

[28]   Gilarranz, J. L., L. W. Traub, and O. K. Rediniotis. "A new class of synthetic jet actuators—Part I: Design, fabrication and bench top characterization." *J. Fluids Eng.* 127, no. 2 (2005): 367-376. https://doi.org/10.1115/1.1839931

[29]   Gilarranz, J. L., L. W. Traub, and O. K. Rediniotis. "A new class of synthetic jet actuators—part II: application to flow separation control." *J. Fluids Eng.* 127, no. 2 (2005): 377-387. https://doi.org/10.1115/1.1882393

[30]   Hwang, W., and J. K. Eaton. "Creating homogeneous and isotropic turbulence without a mean flow." *Experiments in Fluids* 36 (2004): 444-454. https://doi.org/10.1007/s00348-003-0742-6

[31] Variano, Evan A., Eberhard Bodenschatz, and Edwin A. Cowen. "A random synthetic jet array driven turbulence tank." *Experiments in fluids* 37 (2004): 613-615. https://doi.org/10.1007/s00348-004-0833-z

[32] Yamamoto, Kohei, Tomoaki Watanabe, and Koji Nagata. "Turbulence generated by an array of opposed piston-driven synthetic jet actuators." *Experiments in Fluids* 63, no. 1 (2022): 35. https://doi.org/10.1007/s00348-021-03351-z

[33] Yamamoto, K., T. Ishida, T. Watanabe, and K. Nagata. "Experimental and numerical investigation of compressibility effects on velocity derivative flatness in turbulence." *Physics of Fluids* 34, no. 5 (2022): 055101. https://doi.org/10.1063/5.0085423

[34] Qayoum, A., and A. Malik. "Influence of the excitation frequency and orifice geometry on the fluid flow and heat transfer characteristics of synthetic jet actuators." *Fluid Dynamics* 54 (2019): 575-589. https://doi.org/10.1134/S0015462819040086

[35] OpenFOAM, Ver.7 For Ubuntu 16.04LTS, 8th Jul. (2019). https://doi.org/10.18623/rvd.v16i35.1664

[36] Sakakibara, Hiroyuki, Tomoaki Watanabe, and Koji Nagata. "Supersonic piston synthetic jets with single/multiple orifice." *Experiments in Fluids* 59 (2018): 1-12. https://doi.org/10.1007/s00348-018-2529-9

[37] Issa, Raad I. "Solution of the implicitly discretised fluid flow equations by operator-splitting." *Journal of computational physics* 62, no. 1 (1986): 40-65. https://doi.org/10.1016/0021-9991(86)90099-9

[38] Caretto, L. S., A. D. Gosman, S. V. Patankar, and D. B. Spalding. "Two calculation procedures for steady, three-dimensional flows with recirculation." In *Proceedings of the Third International Conference on Numerical Methods in Fluid Mechanics: Vol. II Problems of Fluid Mechanics*, pp. 60-68. Springer Berlin Heidelberg, 1973. https://doi.org/10.1007/BFb0112677

[39] Holzmann, Tobias. "Mathematics, numerics, derivations and OpenFOAM®." *Loeben, Germany: Holzmann CFD* (2016).

[40] Anderson, John David. *Modern compressible flow: with historical perspective*. Vol. 12. New York: McGraw-Hill, 1990.

[41] Yaacob, Mohd Rusdy, Rasmus Korslund Schlander, Preben Buchhave, and Clara Marika Velte. "A novel laser Doppler anemometer (LDA) for high-accuracy turbulence measurements." *arXiv preprint arXiv:1905.08066* (2019).

[42] Yaacob, Mohd Rusdy, Rasmus Korslund Schlander, Preben Buchhave, and Clara M. Velte. "Experimental evaluation of kolmogorov's-5/3 and 2/3 power laws in the developing turbulent round jet." *Journal of Advanced Research in Fluid Mechanics and Thermal Sciences* 45, no. 1 (2018): 14-21.